Fuel 286 (2021) 119353

Contents lists available at ScienceDirect

Fuel

journal homepage: www.elsevier.com/locate/fuel

Full Length Article

Experimental and numerical study on the effect of oxymethylene ether-3 (OME_3) on soot particle formation

Federica Ferraro [a,*], Carmela Russo [b], Robert Schmitz [a], Christian Hasse [a], Mariano Sirignano [c]

[a] Institute for Simulation of Reactive Thermo-Fluid Systems (STFS), Technische Universität Darmstadt, Otto-Berndt-Straße 2, Darmstadt 64287, Germany
[b] Istituto di Ricerche sulla Combustione, Consiglio Nazionale delle Ricerche, P.le Tecchio 80, 80125 Napoli, Italy
[c] Dipartimento di Ingegneria Chimica, dei Materiali e della Produzione Industriale – Università degli Studi di Napoli Federico II, P. le Tecchio 80, 80125 Napoli, Italy

ARTICLE INFO

Keywords:
Oxymethylene ether-3 (OME_3)
Polyoxymethylene dimethyl ether-3 ($PODE_3$)
Soot
Alternative fuels
Quadrature Method of Moments (QMOM)

ABSTRACT

The reduction and control of particulate matter generated by fossil fuel combustion are among the main issues for actual and future combustion devices due to the increasingly stringent emission regulations. Recently, various fuels have been investigated as a potential substitute or additive for diesel and gasoline. This work focuses on how oxymethylene ether-3 (OME_3), the smallest promising OME compound, affects carbon particulate formation when blended with ethylene in burner-stabilized premixed flames at different equivalence ratios. Particle size distribution (PSD) and Laser-Induced Fluorescence (LIF) and Incandescence (LII) along with numerical (Conditional Quadrature Method of Moments – CQMOM, based on D'Anna physico-chemical soot model) investigations were conducted to study particle formation and growth in pure ethylene and ethylene/OME_3 flames. The soot volume fraction and PSD indicate a reduction in the total number and the size of the soot particles at all equivalence ratios, while the number of small nanoparticles remains almost unchanged. The CQMOM model is able to predict similar trends for the soot volume fraction and, using the entropy maximization concept, the general shape of the PSD for both pure ethylene and OME_3-blended flames, compared to the experimental measurements.

Further, carbon particulate matter was thermophoretically sampled in the highest equivalence ratio conditions and spectroscopically analyzed. The soot structure was investigated using UV–Visible and Raman spectroscopy, finding a slightly higher aromaticity for the pure ethylene soot. FTIR analysis showed that carbon particulate matter produced from an OME_3-doped flame contained larger amounts of oxygen, mainly in the form of C═O.

1. Introduction

Soot is a particulate pollutant generated by the incomplete combustion of all hydrocarbons, including oxygenated ones. Due to its carcinogenic effects on human health and its detrimental impact on polar ice melting and climate change, the soot emission limits for combustion devices have become more stringent. Both the soot mass concentration and particle size distribution (PSD) need to be controlled and accurately predicted to design the next generation of combustion devices.

While bigger particles can be filtered with exhaust gas aftertreatment systems, small nanoparticles are more difficult to trap [1] and, once released into the atmosphere, can penetrate deeper into the human respiratory system, causing severe damage [2,3].

In order to reduce the carbon footprint, as well as the particulate emissions of combustion systems, the use of alternative synthetic fuels has been widely explored [4,5]. Oxygenated fuels including molecules that can be mixed with diesel (dimethyl ether (DME), biodiesel, etc.) and gasoline (bioethanol, biobutanol, etc.) have been developed in recent years. The general belief is that due to their intrinsic structure with high levels of embedded oxygen, the decomposition/oxidation of oxygenated fuel molecules is faster and more efficient [5] and lower amounts of particulate pollutants are emitted [6,7]. Despite these advances, recent studies have shown that these fuels indeed have great potential in reducing the total amount of particulate produced and hence emitted; however, particles are produced which are smaller in size [8] and, in some combustion conditions, higher in concentration [4]. Additionally, recent findings have shown that the use of oxygenated fuels can lead to the production of oxy-PAHs (polycyclic aromatic hydrocarbons) [9] and of particles with different chemical features, namely a larger presence of

* Corresponding author.
E-mail address: ferraro@stfs.tu-darmstadt.de (F. Ferraro).

https://doi.org/10.1016/j.fuel.2020.119353
Received 28 May 2020; Received in revised form 23 July 2020; Accepted 26 September 2020
Available online 1 November 2020

oxygen incorporated into particles [6,7,10]. This latter aspect could be responsible for the higher reactivity to oxidation [6,8,11–16] exhibited by the particulate which is formed, resulting in easier abatement in the after-treatment systems, but also in a higher propensity to interact with biological systems, yielding potentially higher toxicity [3]. These controversial aspects have to lead to research into new alternative fuel candidates in order to prevent possible negative outcomes from their use on a large scale.

Among several alternative fuel candidates, oxymethylene ethers (OME_n), $CH_3O(CH_2O)_nCH_3$, also known as polyoxymethylene dimethyl ethers (PODEs), are promising for realizing carbon–neutral combustion, when used as additives or substitutes for diesel engines. OMEs belong to the class of e-fuels, i.e., fuels that can be produced by recycling CO_2 via electrolysis using renewable energies, contributing to the overall greenhouse gas balance [17]. The high oxygen content and the lack of C—C bonds of OMEs generate fewer soot precursors such as C_2H_2, C_2H_4 and C_3H_3, indicating that there could be a potential reduction in carbon particulates [18]. OMEs with $n > 1$ have a high propensity to ignite, with a cetane number exceeding 60 [18]. Additionally, OMEs are non-toxic and miscible in diesel fuel. OMEs have shown positive effects in terms of reducing CO, unburned hydrocarbons and soot particle emissions when used as an additive to diesel in engine experiments [19–25]. A higher rate of exhaust gas recirculation (EGR) can be applied to reduce NO_x emissions [23,26]. Investigations on OME_1 as an alternative fuel indicate that soot is suppressed entirely [27]. However, since severe modifications are required for the engine and fuel supply system, blending OMEs into diesel fuels is a more feasible strategy.

Previous studies have identified OME_3 as the smallest-sized OME_n compound qualified for practical applications [18]. It has a high cetane number equal to 78, a low melting point at −41 °C and a high boiling point at 156 °C [24]. Examining the physico-chemical properties of the other OME_n compounds [18,24] it can be determined that: OME_1 has a low cetane number (29) and low boiling point (42 °C), therefore it is highly volatile and can vaporize during storage; OME_2 has a suitable cetane number (63), but a too low flash point to satisfy safety criteria [28]; OME_4 has a cetane number of 90, a melting point of −7 °C and a boiling point of 202 °C. Additionally, OMEs with $n > 5$ have a too high melting point. In summary, optimal compounds for blending with traditional fuels have $n = 3-4$ or $n = 3-5$ [18]. When OME_3 is compared with OME_4 and OME_5, OME_3 has a better low-temperature fluidity and volatility; therefore, it has been investigated in this study. In future, attention will be devoted to larger OME compounds and their blends.

Recently, reduced and detailed kinetic mechanisms have been developed for $OME_{1\text{-}3}$ [18,29,30] and for $OME_{2\text{-}4}$ [17], validated against experimental data on the ignition delay time [17,18] and laminar flame speed [29]. The sooting propensity of OME/diesel blends in diffusion flames has been studied in [31] and a reduction in soot was found when OME compounds are added.

Following previous studies on other alternative fuels [6,7,10,32–36], the primary goal of this work is to characterize the sooting properties of OME_3 used as an additive in ethylene/air flames at different equivalence ratios [37]. In order to evaluate the effect of OME_3 and to identify some specific patterns related to the fuel structure, both experimental and numerical investigations are performed. To the best of our knowledge, there are no comprehensive studies on sooting behavior in laminar flames when OME_3 is used for blending other fuels. Experimental investigations include quantitative measurements of particulate both in situ (laser-based technique) and ex situ (particle size distribution measurements), and the characterization of particulate (UV–Visible (UV–Vis), Raman, FTIR analysis) in terms of its composition and nanostructure. Simulations are performed with the detailed physico-chemical soot model proposed by D'Anna et al. [38,39] integrated into a Conditional Quadrature-based Method of Moments (CQMOM) approach [40,41]. Different types of species such as large PAHs, clusters and agglomerates are accounted for in the soot model, as well as dehydrogenation and oxidation-induced fragmentation processes. $OME_{1\text{-}3}$ kinetics from Sun et al. [29] has been included in the gas-phase kinetic mechanism to account for the fuel mixture oxidation. Classical CQMOM methods are not able to approximate the PSD directly, and the Extended Quadrature Method of Moments [42–44] has recently been introduced to cope with this problem. Below [41], an alternative approach based on the entropy maximization concept is employed here, which allows the PSD to be reconstructed, given a suitably selected set of transported moments.

2. Experimental setup

Premixed ethylene/air flames at atmospheric pressure and with equivalence ratios, ϕ, equal to 2.01, 2.16, 2.31 and 2.46 are stabilized on a capillary burner (inner diameter of 5.8 cm) by means of a stainless steel plate located 30 mm above the burner surface. These flames are the reference cases for studying the effect of OME_3 blending on particle formation and growth. OME_3 was fed in by means of a syringe pump and pre-vaporized by the preheated ethylene/oxygen/nitrogen stream (150 °C). OME_3 was added by replacing some of the ethylene (20% of the total carbon) fed to the reference ethylene/air flames. The equivalence ratio, the cold gas velocity and the total carbon flow rate were kept constant while OME_3 was added. In order to achieve this, the nitrogen and oxygen streams were adapted accordingly. The combustion conditions investigated in this work are reported in Table 1. The same approach and experimental setup have been used for studying other alternative fuels such as butanols [10], furans [33], ethanol [34], and dimethyl ether [36].

Flame temperatures were not measured for OME_3/ethylene flames, whereas temperature profiles were available for pure ethylene flames [10]. However, by keeping the combustion parameters constant as described above, the effect of OME_3 on the flame temperature was considered to be negligible, similarly to the case of other alternative fuels [33]. The temperature profiles for pristine flames were used as an input for the modeling. In these conditions, the chemical effect of OME_3 on particle formation is isolated from the thermal effect.

The experimental setup for optical and particle size distribution, as well as the method of collecting particulate on a glass plate, are the same adopted in previous works (see [10,33,35]). Below, a brief description is given for completeness.

Laser-Induced Emission (LIE) measurements in the 200–550 nm range were used to detect particles in the flame, using the fourth harmonic of a Nd:YAG laser at 266 nm as the excitation source [32,35–37]. The emitted spectra were collected with an ICCD camera with a gate of 100 ns, allowing to distinguish between the broad Laser-Induced

Table 1
Flame conditions. Inflow mixture composition is given in mole fraction. Inlet Gas velocity @STP = 10 cm/s.

ϕ	% OME_3	0	20
2.01	C_2H_4	0.1234	0.0987
	O_2	0.1841	0.1767
	N_2	0.6925	0.7147
	OME_3	0	0.0099
2.16	C_2H_4	0.1313	0.1051
	O_2	0.1824	0.1751
	N_2	0.6862	0.7093
	OME_3	0	0.0105
2.31	C_2H_4	0.1392	0.1114
	O_2	0.1808	0.1735
	N_2	0.68	0.704
	OME_3	0	0.0111
2.46	C_2H_4	0.1469	0.1175
	O_2	0.1792	0.172
	N_2	0.6739	0.6987
	OME_3	0	0.0118

Fluorescence (LIF) signal, ranging between 300 and 450 nm, and the Laser-Induced Incandescence (LII) following a blackbody curve and evaluated at 550 nm.

In order to retrieve information on the PSD, particle sampling from the flames was performed with a horizontal probe [45–50]. The horizontal probe adopted here has an inner diameter of 8 mm, a wall thickness of 0.5 mm, and a pinhole diameter of 0.8 mm. This very large pinhole was set up here with a two-stage dilution system: the carrier gas was set to 4 Nl/min (at 273 K) for the first dilution and to 65 Nl/min in the second dilution stage [32,37,45]. An overall dilution of 500 was achieved.

Particles sampled from the flame were sent to a nano-Differential Mobility Analyzer (DMA) (TapCon 3/150 DMA system with a nominal size range of 2–100 nm, equipped with a Faraday Cup Electrometer detector). In order to charge the particles to Fuchs' steady-state charge distribution [51], a Soft X-Ray Advanced Aerosol Neutralizer (TSI model 3088) was used. The PSDs were obtained by averaging over 3 scans and resulting uncertainty is reported as error bars. The PSDs obtained by DMA were corrected for losses in the pinhole and the probe, following the procedure reported in the literature [52–54]. DMA separates particles based on their mobility diameter, so the particle diameter could be retrieved from the correlation proposed by Singh et al. [55]. Nano-DMA errors originate in the fluctuation of the suction pressure, the partial clogging of the orifice due to soot deposition at high equivalence ratios, wall losses and the coagulation of small particles onto large ones. Hence, the largest uncertainties concern the smallest particles.

A 75 × 25 × 1 mm glass plate was horizontally inserted into the flame for 2 s to collect material from the flame at the highest equivalence ratio. The operation was repeated several times with a cooling cycle at room temperature of 10 s after each insertion. The procedure has been tested and validated before [7,56]. Spectroscopic techniques were used to characterize the sampled material, similarly to what has been done for particles collected in flames fueled with other oxygenated fuels [33] and benzene [56].

Raman spectra were measured directly on the carbon samples deposited on a glass plate using a Horiba XploRA Raman microscope system (Horiba Jobin Yvon, Japan) equipped with a frequency-doubled Nd:YAG solid-state laser (λ = 532 nm) [33]. Raman spectra analysis provides information on the features of the carbon network. FTIR and UV–Vis spectroscopy were performed on the samples removed from the glass plate. FTIR spectra in the 3400–600 cm^{-1} range were acquired in the transmittance mode using a Nicolet iS10 spectrophotometer. For FTIR analysis, the sample needs to be prepared; in particular, carbon particulate matter samples were mixed and ground in KBr pellets (0.2–0.3 wt%) [57]. FTIR gives information on the presence of oxygen within the carbon network. For the UV–Vis analysis, carbon particulate matter samples were suspended in N-methyl-2-pyrrolidone (NMP, with a concentration of 10 mg/L) and analyzed in a 1-cm path length quartz cuvette using an Agilent UV–Vis 8453 spectrophotometer. The UV–Vis spectra were also measured on the soot fraction < 20 nm obtained by filtration on an Anotop filter (Whatman) of a 100 mg/L total particulate suspension. UV–Vis analysis provides information on the mass absorption coefficients for the particles sampled, indicating the level of aromaticity.

Each sampling point was repeated at least three times. Each sample for each experimental condition was preliminarily analyzed using Raman spectroscopy to ensure the sampling reproducibility. After this check, the samples were added together for further spectroscopic analysis. The experimental error for Raman and UV–Vis spectroscopy measurements was evaluated as being less than 5%, whereas for FTIR spectroscopy the error was less than 10%.

3. Numerical modeling

3.1. Gas phase kinetic mechanism and soot model

A detailed kinetic mechanism is used in this work, which includes the kinetic mechanism developed by D'Anna and coworkers [33,38,39,58] and the $OME_{1\text{-}3}$ kinetics taken from Sun et al. [29]. The entire mechanism consists of 141 species and 674 reactions, of which 41 species and 213 reactions are added to include the $OME_{1\text{-}3}$ oxidation kinetics [29].

The physico-chemical soot formation model employed in this work [38] has been combined with the CQMOM approach to track the particulate evolution in [40] and successfully applied for simulating lightly and highly sooting flames in [40,41]. The present model distinguishes between different particle structures based on their state of aggregation, i.e. high-molecular-mass aromatic molecules (*molecules or large PAHs*), clusters of molecules (*clusters*) and agglomerates of particles (*aggregates*) [38]. This allows not only the mass of the formed particles to be followed, but also their hydrogen content and internal structure. Oxidation-induced fragmentation is also accounted for. Oxygen is considered the only species which can avoid reaction on the surface and diffuse towards the points of contact of the primary particles, causing internal oxidation and subsequent particle fragmentation. PAH formation is modeled by the H-Abstraction-C_2H_2-Addition (HACA) route and the resonantly stabilized free radical (RSFR) mechanism [38], while the molecular growth is described from benzene up to pyrene. All the PAH compounds with a molecular weight larger than pyrene are not treated as individual species but considered as lumped species (*large PAHs*), whose evolution is described by the CQMOM. If the Van der Waals forces are strong enough to hold together these large molecules, *clusters* are formed. *Clusters* can grow via chemical pathways and can interact through coagulation. When larger clusters are formed, coagulation becomes an aggregation process, forming chain-like soot particles (*aggregates*). Their reactions are described based on similarity with gas-phase kinetics following Arrhenius-rate laws.

3.2. CQMOM model

Large hydrocarbons and particulates which are not directly solved in the gas-phase kinetics are described by the evolution of the population balance equation (PBE) for the number density function (NDF) $f\left(\underline{\xi};\underline{x},t\right)$. Here, $\underline{x}$ is the space vector, t is the time, and $\underline{\xi}$ is the internal coordinate vector defined as $\underline{\xi} = \left[\xi_{nc},\xi_{H/C},\xi_{stat},\xi_{typ}\right]^T$, where ξ_{nc} is the number of carbon atoms, with $\xi_{nc} \in [0,\infty)$, $\xi_{H/C}$ is the H/C ratio with $\xi_{H/C} \in [0,1]$, ξ_{stat} represents the state of the particular entity with $\xi_{stat} \in A, A = \{stable, radical\}$, and ξ_{typ} is the type of the entity with $\xi_{typ} \in B, B = \{largePAHs, clusters, agglomerates\}$. Note that the four coordinates are independent of one other, and the two coordinates ξ_{stat} and ξ_{typ} are discrete in nature. Using the concept of the conditional density function allows the quadrivariate NDF to be written as

$$f\left(\underline{\xi}\right) = f_{H/C}\left(\xi_{H/C}|\xi_{nc},\xi_{stat},\xi_{typ}\right)\cdot f_{nc}\left(\xi_{nc}|\xi_{stat},\xi_{typ}\right)\cdot n\left(\xi_{stat},\xi_{typ}\right), \quad (1)$$

where $\underline{x}$ and t dependencies are dropped for convenience. Here, $f_{H/C}$ represents the distribution of $\xi_{H/C}$ conditioned on a certain state $(\xi_{nc}, \xi_{stat}, \xi_{typ})$ and f_{nc} represents the distribution of ξ_{nc} conditioned on a state (ξ_{stat}, ξ_{typ}). The joint bi-variate distribution $n\left(\xi_{stat},\xi_{typ}\right)$ can assume only six different values, one for each possible combination (u,v) of their discrete domain parameters $\xi_{stat} = \xi_{stat,u}$, $\xi_{typ} = \xi_{typ,v}$. Therefore, evaluating $n\left(\xi_{stat},\xi_{typ}\right)$ at the six discrete points (u,v) allows the quadrivariate $f\left(\underline{\xi}\right)$ to be reformulated as a set of six bivariate NDFs $\Pi_{u,v}$

$$\Pi_{u,v}\left(\xi_{nc},\xi_{H/C}\right) = f^{u,v}_{H/C}\left(\xi_{H/C}|\xi_{nc}\right)\cdot f^{u,v}_{nc}\left(\xi_{nc}\right)\cdot n_{u,v}, \quad (2)$$

where $f^{u,v}_{H/C}\left(\xi_{H/C}|\xi_{nc}\right)$ is a conditional NDF, $f^{u,v}_{nc}(\xi_{nc})$ is a marginal NDF depending only on ξ_{nc} and $n_{u,v}$ is the number density for each combination of (u,v). This is numerically convenient for the moment-based CQMOM approach used in this work. However, the six bivariate distributions $\Pi_{u,v}$ are not independent of each other, but strongly coupled by

different source terms, e.g. the condensation of large PAHs on agglomerates, which modifies both NDFs. A complete description of the coupling approach is described in [40]. Similarly to [41], transport equations for the fractional moments $m_{u,v}^{\frac{k_1}{z},k_2}$ of the six bivariate NDFs in Eq. (2) are solved

$$m_{u,v}^{\frac{k_1}{z},k_2} = \int_0^\infty \int_0^1 \xi_{nc}^{\frac{k_1}{z}} \xi_{H/C}^{k_2} \Pi_{u,v}(\xi_{nc}, \xi_{H/C}) \mathrm{d}\xi_{H/C} \mathrm{d}\xi_{nc}. \quad (3)$$

In the present study, fractional moments with $z = 3$ are used for the property ξ_{nc}.

The moment inversion procedure for fractional moments in the CQMOM context has been extended in [41] and is used here. When the moment inversion is completed, the $N_{\xi_{nc}}$ quadrature nodes $\xi_{nc,i}^{1/3}$ and weights $w_{nc,i}$ for the coordinate ξ_{nc}, and the $N_{\xi_{H/C}}$ conditional nodes $\xi_{H/C,i,j}$ and weights $w_{H/C,i,j}$ for the coordinate $\xi_{H/C}$, for each combination (u,v), are employed to determine the unclosed moment source terms for all the physical and chemical processes described in [38] and treated here in a lumped formulation [40,41]. Two-way coupling between the soot phase and the gas phase is considered. The molecular diffusion of soot is neglected, as well as the thermophoresis, which is known to have negligible effects in premixed flames [59].

Following Salenbauch et al. [41], the entropy maximization (EM) concept is employed in post-processing to evaluate the PSD, without prescribing the distribution shape. It is noteworthy that solving for the fractional moments offers the advantage of being able to directly evaluate the PSD, applying the EM concept. Indeed, using the relation between the equivalent-volume sphere diameter d_p and the coordinate ξ_{nc}

$$d_p = \left(\frac{6W_c}{\pi\rho_s}\right)^{1/3} \xi_{nc}^{1/3} = L^{1/3} \xi_{nc}^{1/3}, \quad (4)$$

with W_c the mass of a single carbon atom and ρ_s the soot density, the transported fractional moments $m_{u,v}^{\frac{k_1}{3},0}$ can be directly transformed into diameter-based moments $\langle m_{u,v}^{k_1} \rangle$

$$\langle m_{u,v}^{k_1} \rangle = \int_0^\infty d_p^{k_1} f_{d_p}(d_p) \mathrm{d}d_p = L^{k_1/3} \int_0^\infty \xi_{nc}^{k_1/3} f_{nc}(\xi_{nc}) \mathrm{d}\xi_{nc} = L^{k_1/3} m_{u,v}^{\frac{k_1}{3},0}. \quad (5)$$

The diameter-based moments are then employed with the EM concept to evaluate the NDF $f_{d_p}(d_p)$ at each location in the domain. Further details can be found in [40,41].

4. Results and discussion

Burner-stabilized ethylene/air and ethylene/OME$_3$/air flames with different equivalence ratios ϕ (see Table 1) are investigated both experimentally and numerically. One-dimensional simulations have been performed imposing temperature profiles measured in the experiments for the pure ethylene flames at different equivalence ratios.

Thus, the same temperature profiles are used at each equivalence

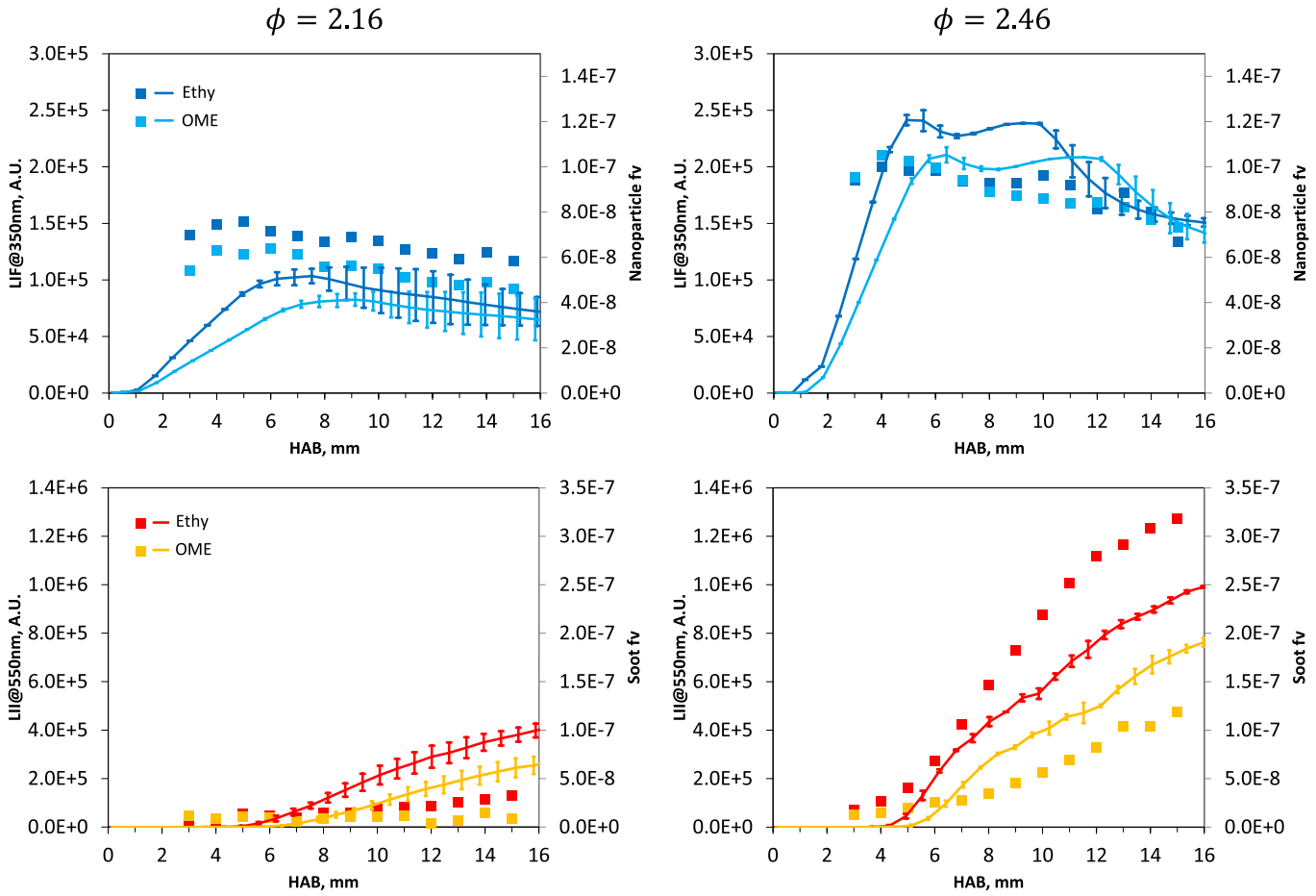

Fig. 1. Comparison of the soot volume fraction predicted by the model with the experimental measured LIF signal (top) and LII signal (bottom) for $\phi = 2.16$ (left) and 2.46 (right) flames: ethylene/air (blue line and symbols: LIF; red line and symbols: LII), ethylene/OME$_3$/air (cyan line and symbols: LIF; orange line and symbols: LII). A separation is carried out for the particles calculated by CQMOM based on the PSD reconstruction with EM: for LIF, $d_p < d_{p,split}$, for LII, $d_p > d_{p,split}$. Error bars indicate the sensitivity with respect to the value of $d_{p,split}$ in the range of 2 nm $\leq d_{p,split} \leq$ 7 nm. (For interpretation of the references to colour in this figure legend, the reader is referred to the web version of this article.)

ratio for flames of pure ethylene and with added OME_3. The CQMOM-based soot model is applied to solve the PBE for large PAHs, particle clusters and agglomerates. Two quadrature nodes for ξ_{nc} and one quadrature node for $\xi_{H/C}$ conditioned on each ξ_{nc} node for all of the six combinations (state, type) are used, leading to a total of 36 moment transport equations. A variable soot density ρ_s is considered between 1000 and 1800 kg/m^3 as an inverse function of the H/C ratio. It is worth underlining the fact that the simulations are performed without tuning or modifying the model parameters for the different equivalence ratios and fuel mixtures.

4.1. Soot evolution

In Fig. 1, the comparison between LIF and LII signals and the respective simulated volume fraction is only qualitative and reported for two equivalence ratios: 2.16 and 2.46. It is worth noting that the pure ethylene flame at an equivalence ratio of 2.16 is the first flame condition where LII has been detected above the noise level.

According to previous studies, LIF signals here are attributed to aromatic hydrocarbons in condensed-phase nanostructures that are not able to incandesce (see [2,37] and references therein). This attribution significantly affects the selection of adequate species from the modeling results for comparison with the LIF signal. In previous works, the LIF signal has been assumed to be directly related to the formation of condensed-phase nanostructures, i.e. particles with diameters of $d_p \leq$ 7 nm [41], while the detection of the LII signal indicates the presence of larger particles [10]. Following [41], the simulated PSD obtained with CQMOM and EM, as described in Section 3.2, is split in a post-processing step to account for small particles with diameters of $d_p < d_{p,split}$ and larger particles with $d_p > d_{p,split}$, for comparison with the LIF and LII signals, respectively. The value of the split diameter was varied within the relevant range of 2 nm $\leq d_{p,split} \leq$ 7 nm and the results are indicated by the error bars in Fig. 1. The CQMOM model is able to predict a substantially unchanged volume fraction of small particles (as from LIF) when OME_3 is added for both equivalence ratios shown in Fig. 1 (top).

Furthermore, the simulations are able to reproduce the trend of large particles having an increasing volume fraction (as from LII in Fig. 1) as the equivalence ratio increases, and their volume fraction decreasing when OME_3 is added. The simulations predict a delay in the onset of small particles, which suggests that OME_3 affects their formation process. Similarly to the large particle aggregates, the effect of OME_3 is linked to a delay in the onset and particle growth. More specifically, this is due to the lower abundance of particle gas-phase precursors, such as PAHs, and different concentrations of other important species such as C_2H_2, which is responsible for surface growth at high equivalence ratios. The simulations predict a lower reduction in large particles than that observed in experiments, which can be seen particularly clearly in the richest conditions investigated at $\phi = 2.46$.

The effects of OME_3 shown so far have been similarly observed in ethylene flames doped with other oxygenated compounds such as ethanol [35], dimethyl ether [36], butanols [10] and furans [33]. This suggests, as for the other fuels, that the particle reduction must mainly be attributed to the modification of gas-phase precursors when OME_3 is added. Hence it is possible that the gas-phase model adopted here, developed mostly in a low-pressure environment [29], needs to be updated to predict gas-phase compounds.

Fig. 2 shows the PSD measured at a height above the burner (HAB) of 15 mm for the four equivalence ratios investigated, with and without the

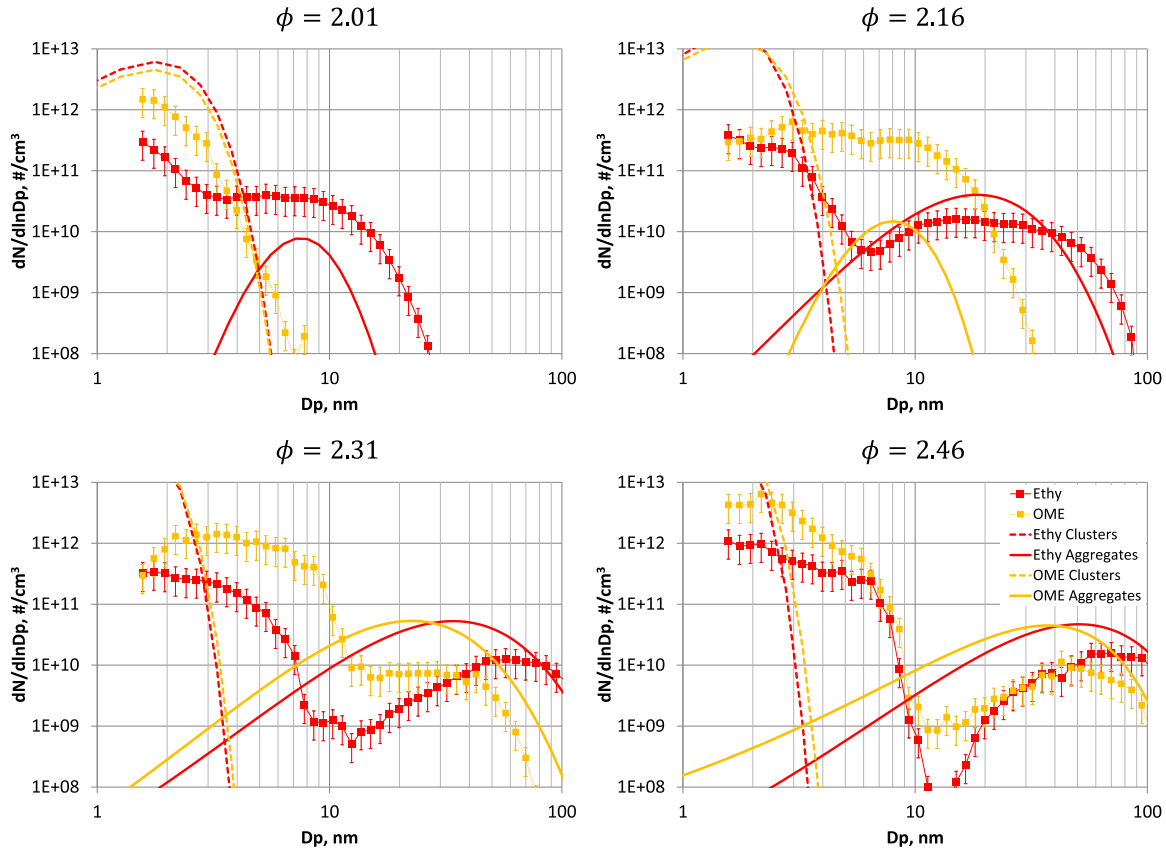

Fig. 2. Particle size distributions determined with EM on the CQMOM simulation results compared with the experimental measurements (SMPS) at HAB = 15 mm for flames with different equivalence ratios of 2.01, 2.16, 2.31 and 2.46: ethylene/air (red line and symbols), ethylene/OME_3/air (orange line and symbols). Dashed lines indicate the clusters and solid lines the aggregates. (For interpretation of the references to colour in this figure legend, the reader is referred to the web version of this article.)

addition of OME_3. The measurements are compared with the predicted PSD from the EM procedure applied to CQMOM flame solutions. For soot particle aggregates, the simulated PSDs are plotted versus the mobility diameter d_m, here equal to the collision diameter d_c as in [60], $d_m \equiv d_c = d_p n_p^{1/D_f}$, where n_p is the number of primary particles in an aggregate calculated on the base of the ratio between the mass of the aggregate and the mass of the primary particle. In this work, the fractal dimension D_f is assumed to be equal to 1.8 and the primary particle diameter d_p to be equal to 15 nm for all the investigated conditions to avoid altering the assessment of the model performance. It is worth underlining that the correlation has been used in order to provide a direct comparison between the simulation results and the data coming from the nano-DMA. Since calculating the mobility diameter from the mass can be difficult, here the aim of the comparison is to show the output of the model. The chosen parameters can be considered reasonable compared with the average values used in the literature [60].

In Fig. 2 it can be observed that for slightly sooting conditions with $\phi = 2.01$, adding OME_3 changes the shape of the PSD from bimodal to unimodal. A bimodal PSD remains evident, instead, for higher equivalence ratio conditions. An additional effect of the OME_3 blending is that a slightly higher number of small particles with $d_p < 5$ nm is formed, while the number of larger particles with $d_p > 20$ nm is drastically reduced at all equivalence ratios.

The modeled PSDs indicate that all the relevant effects of adding OME_3 described above are captured qualitatively. In particular, the model is able to reproduce the trend of increasing size and the total amount of aggregates at increasing equivalence ratios, and a substantially unchanged total number concentration of particles smaller than 10 nm. However, the number concentration of small particles is overpredicted at all equivalence ratios. It has been also reported above and in previous work [37,61] that the SMPS measurements may be affected by significant losses of small particles.

The reduction in the total number of particles produced and the minor or even enhancing effect of small particles is in line with the other oxygenated fuels studied in the same conditions [10,33–36]. The absence of C—C bonds as in DME leads to an even more significant, faster decomposition/oxidation and thus a reduction in gas-phase precursors including PAHs and C_2H_2. As for other investigated biofuels, the presence of oxygenated molecules in fuel streams does not alter the process leading to particle formation, which mostly affects the main gas phase pathways. However, the formation of a small/trace amount of particular compounds – such as oxy-PAHs or other oxygenated large molecules – which may not even play a role in determining the total number of particles or the PSD – can significantly alter the features of the particles produced (see Section 4.2).

4.1.1. Modeling tests

In order to further investigate the importance of the different kinetic pathways that lead to the gas-phase decomposition of OME_3 and its role in particle formation, a numerical experiment was performed. OME_3 was numerically fed into the flame, decomposed into smaller hydrocarbons, to simulate fast decomposition towards the final products. The richest condition ($\phi = 2.46$) was chosen for this study since the largest discrepancy with the experimental data in terms of soot reduction was found in this context (see Fig. 1). In particular, three possible cases were analyzed.

$$OME_3 \Rightarrow 4\ CH_2O + CH_4 \quad \text{(Case 1)}$$

$$16\ OME_3\ (+39\ O_2) \Rightarrow 80\ CO + 34\ H_2 + 62\ H_2O \quad \text{(Case 2)}$$

$$OME_3\ (+6\ O_2) \Rightarrow 5\ CO_2 + 6\ H_2O \quad \text{(Case 3)}$$

It is possible to see that Case 1 is pure decomposition whilst the others are decomposition plus partial oxidation (Case 2) or complete oxidation (Case 3). In all the decompositions, the cold gas velocity was kept the same by adjusting the nitrogen flow rate and, overall, the same number of moles of C, H, and O were fed into the system. In fact, when OME_3 was considered partially or fully oxidized, the oxygen in the fed stream was adjusted accordingly. For the sake of clarity, in Table 2 the molar fractions of the streams in the decomposed tests are reported together with the base case. The temperature profile was kept equal to the base case in order to evaluate only the chemical effects.

In Case 1, OME_3 was decomposed into 4 molecules of CH_2O and 1 molecule of CH_4; this is the simplest possible decomposition and simulates the fast breaking of the C—O bonds. In Case 2, OME_3 was broken and partially oxidized: all the carbon atoms coming from OME_3 were considered to be partially oxidized to CO, the hydrogen atoms coming from OME_3 were fed both as H_2 and H_2O. The amount of H_2 converted to H_2O was decided by leaving the remaining ethylene burning with $C_2H_4/O_2 = 0.82$ (i.e. ϕ for the ethylene equal to 2.46 – see Table 2). This decomposition simulates the capability of OME_3 to go towards partially oxidized products. Finally, in Case 3, OME_3 is considered to be fast enough to go towards the fully oxidized products and OME_3 is decomposed in CO_2 and H_2O. The selected pathways are used here to indicate whether considering a faster oxidation of the OME_3 results in a further reduction of particles formed with respect to the current mechanism.

In Fig. 3, modeling results for the base case and the three decomposition cases are reported in comparison with experimental data: the comparison with LIF is reported in the upper panel and the comparison with LII in the lower panel. It is possible to see that not all decomposition cases lead to an increase in particle reduction. In particular, when OME_3 is decomposed into smaller, highly reactive hydrocarbons (CH_2O and CH_4, the blue line in Fig. 3), the results do not significantly differ from the base case. This suggests that OME_3 decomposition – according to the kinetic scheme adopted here – is already fast enough to form small hydrocarbons. The lower increase may be associated with the higher propensity to form the radicals for molecular growth associated with CH_2O.

Looking at the second decomposition (the green line in Fig. 3), the reduction of both the nanoparticles and soot particles with respect to the base case is significant. In this case, the presence of stable species (CO and H_2) is chemically slowing down the molecular growth process (radicals are less abundant).

Finally, when OME_3 is decomposed and fully oxidized, and CO and H_2O are thus added to the system (the red line in Fig. 3), an increase in particle production is observed. The increase in particle formation has to be linked to the fact that the remaining ethylene and oxygen are burning in a much richer environment, even though it is diluted by CO_2 and H_2O. The increase in the equivalence ratio overwhelms the dilution effect and the chemical effect of CO_2 and H_2O that would lead to a reduction in the number of particles.

Overall, the numerical tests suggest that the kinetic scheme used in

Table 2
Flame conditions for the decomposition cases with equivalence ratio $\phi = 2.46$. Inflow mixture composition is given in mole fraction. Inlet gas velocity @STP = 10 cm/s.

	Base case OME_3	Case 1 $CH_2O + CH_4$	Case 2 $CO + H_2 + H_2O$	Case 3 $CO_2 + H_2O$
C_2H_4	0.1175	0.1175	0.1175	0.1175
O_2	0.172	0.172	0.1433	0.1015
N_2	0.6987	0.6517	0.6099	0.6517
OME_3	0.0118	–	–	–
CH_4	–	0.0118	–	–
CH_2O	–	0.047	–	–
CO	–	–	0.0588	–
H_2	–	–	0.025	–
CO_2	–	–	–	0.0588
H_2O	–	–	0.0455	0.0705
C, mmol/s	**2.97**	**2.97**	**2.97**	**2.97**
H, mmol/s	**6.18**	**6.18**	**6.18**	**6.18**
O, mmol/s	**3.96**	**3.96**	**3.96**	**3.96**

this work is probably underestimating the capability of OME_3 to go towards partially oxidized products. It is possible that in conditions with a medium-high temperature and oxygen-rich environment – such as in the preheating zone of the investigated flame – a faster/direct formation of partially oxidized products could be favored. Future analysis and comparison with experimental data on gas-phase products could help to shed light on this point.

4.2. Soot structure analysis

A detailed spectroscopic analysis of the thermophoretically collected samples was performed to verify how OME_3 affected particulate properties. The analysis was carried out on carbon particulate matter collected on a glass plate at 15 mm HAB and $\phi = 2.46$ in the pure ethylene and ethylene/OME_3 flames. UV–Vis spectroscopy was performed on NMP suspensions with a known concentration of carbon particulate matter removed from the glass plate. UV–Vis mass absorption coefficients in the 250–900 nm range are reported in Fig. 4. The spectrum of particles sampled in the ethylene/OME_3 flame in comparison with that measured for the ethylene flame presents slightly lower mass absorption coefficient values, indicative of a lower aromaticity. On the other hand, the UV–Vis spectrum values of the soot fraction < 20 nm filtered from the total ethylene/OME_3 particulate appear more intense with respect to those measured for the pure ethylene flame, as shown in Fig. 5. In view of the similarity in terms of the shape of the bulk absorption spectra reported in Fig. 4, the lower absorption intensity for the ethylene/OME_3 flame can be justified by the greater abundance of the less light-absorbing particles < 20 nm [62] in this flame, as also confirmed by PSD reported in Fig. 2.

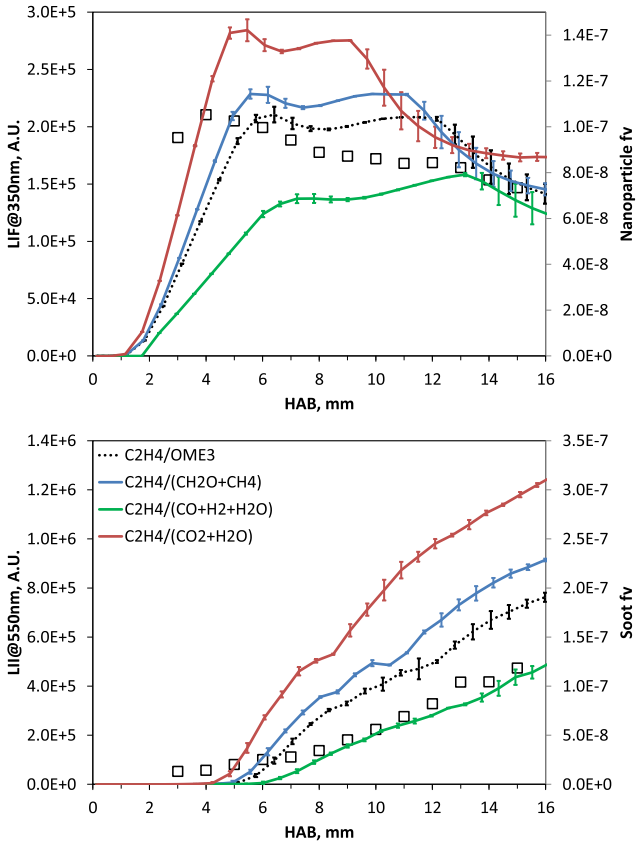

Fig. 3. Comparison of soot volume fractions predicted by the model with the experimentally measured LIF signal (top) and LII signal (bottom) for $\phi = 2.46$ flames of ethylene/OME_3/air (empty symbols). The differently colored continuous lines represent modeling results for the decomposition cases as reported in Table 2, with the dotted line representing modeling results for the base case. A separation is carried out for the particles calculated with CQMOM based on the PSD reconstruction with EM: for LIF, $d_p < d_{p,split}$, for LII, $d_p > d_{p,split}$. Error bars indicate the sensitivity to the value of $d_{p,split}$ in the range of 2 nm $\leq d_{p,split} \leq$ 7 nm. (For interpretation of the references to colour in this figure legend, the reader is referred to the web version of this article.)

The upper panel of Fig. 6 reports the first-order region of the Raman spectra of particles sampled in ethylene and ethylene/OME_3 flames. The spectra present the typical features of disordered/amorphous carbons: a G peak at 1600 cm^{-1} (vibration mode associated with the in-plane bond-stretching motion of pairs of C sp^2 bonds), and a D peak at 1350 cm^{-1} linked with the disorder present in the carbon network [63]. The spectra have been normalized at the G peak to allow an immediate comparison of the spectral features. The G peak position is seen to be higher for the particulate collected in the OME_3/ethylene. It should be remembered that, whatever the excitation energy, the G peak position has a fixed value of 1580 cm^{-1} in perfect and infinite graphite crystals [63], shifted upward to 1600 cm^{-1} for microcrystalline graphite due to the finite crystal size [63]. The G peak position in carbon materials can be shifted up from the 1600 cm^{-1} band limit of purely graphitic carbon by the presence of shorter sp^2 C—C bonds, featuring olefinic bonds and/or small aromatic layers ([64,65]). Thus, the higher G peak position of OME_3/ethylene soot (1606 cm^{-1}) in comparison to pure ethylene soot (1600 cm^{-1}) suggests a higher abundance of olefinic bonds (i.e. a lower abundance of sp^2 aromatic carbon) and/or smaller aromatic layers.

The ratio of the D to the G peak intensity, I(D)/I(G), is the main Raman parameter used for quantifying order/disorder, giving a quantitative measure of the size of the aromatic sp^2 phase organized in clusters. For highly disordered carbons, characterized by an aromatic cluster size smaller than 2 nm, the I(D)/I(G) ratio increases linearly with the crystal area following the equation proposed by Ferrari and Robertson [63].

As can be seen from the upper part of Fig. 6, the spectrum of the OME_3/ethylene soot is characterized by a slightly lower intensity of the I(D)/I(G) ratio. Along with the slightly high position of the G peak, this demonstrates that the average aromatic island size within the carbon network in the ethylene/OME_3 particles is smaller. This suggests that the addition of OME_3 slows soot aromatization and growth. These features can be associated with the generally smaller sizes of particles collected in ethylene/OME_3 flame with respect to pure ethylene flames. A shift of PSD towards small particles indicates a slowing of the growth process that can also be associated with a lower level of aromatization.

Finally, to verify the effect of OME_3 on the composition of carbon particles, FTIR spectroscopy was performed to identify the functional groups of soot particles [57]. The spectra were measured in the same conditions, i.e. the same carbon concentration within the KBr disk and disk thickness, to compare the results. More details on the sample

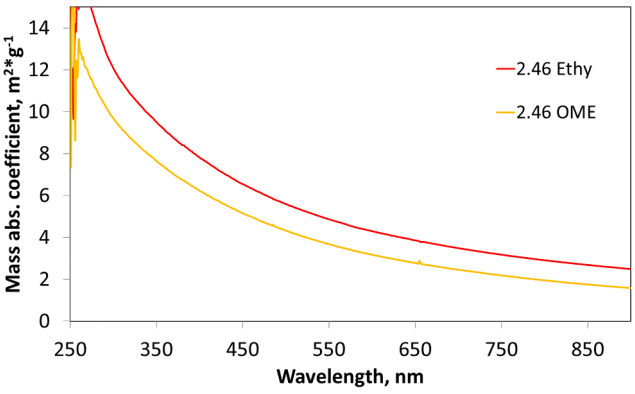

Fig. 4. UV–Vis mass absorption coefficient of particulate collected at 15 mm HAB in the ethylene/air flame (red line) and ethylene/OME_3/air flame (orange line) at $\phi = 2.46$. (For interpretation of the references to colour in this figure legend, the reader is referred to the web version of this article.)

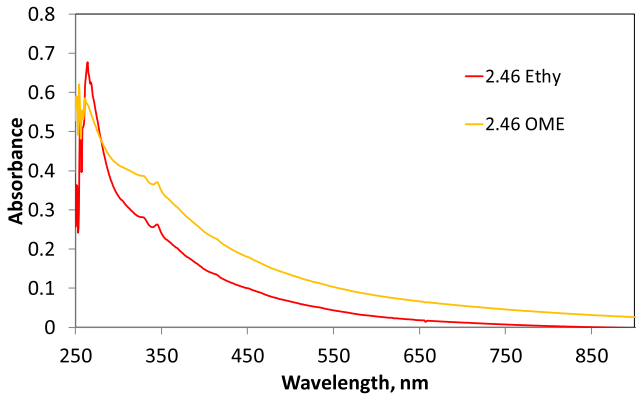

Fig. 5. UV–Vis absorption spectra of the filtered fraction (< 20 nm) of 100 ppm of total particulate collected at 15 mm HAB in the ethylene/air flame (red line) and ethylene/OME_3/air flame (orange line) at $\phi = 2.46$. (For interpretation of the references to colour in this figure legend, the reader is referred to the web version of this article.)

preparation for FTIR measurements are available elsewhere [57].

The spectra in the FTIR spectral region 4000–2500 cm^{-1} where OH stretching peaks (around 3500 cm^{-1}) and CH stretching peaks (3100–2800 cm^{-1}) occur do not exhibit any significant differences, and for this reason they are not reported. Thus, no significant differences in terms of hydrogen content were found, differently from our previous studies on flames doped with 2,5-dimethylfuran [7] and ethanol [6]. This confirms that the main features of the particles produced in pure ethylene and ethylene/OME_3 flames can be considered to be quite similar.

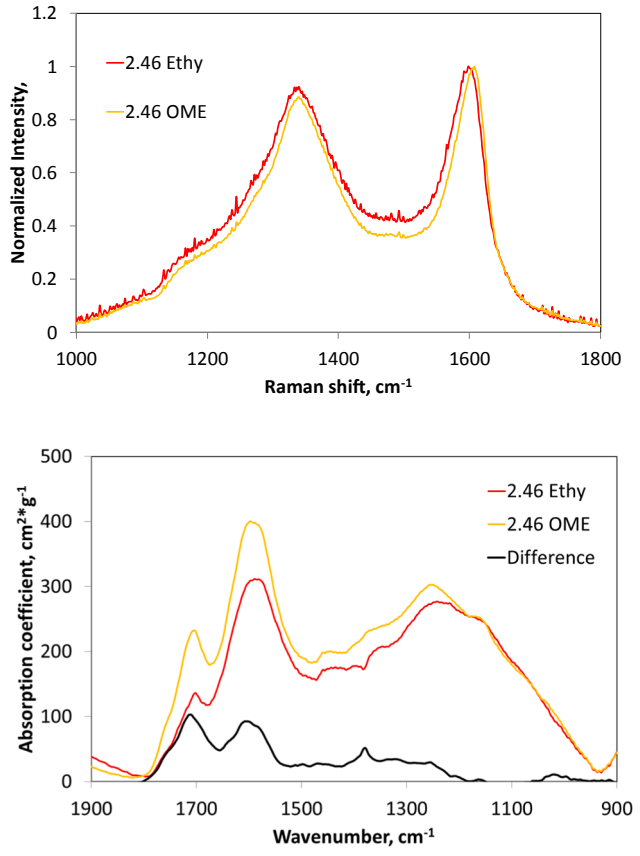

Fig. 6. Raman spectra (top) and infrared mass absorption coefficients (bottom) of soot particles sampled at 15 mm HAB and $\phi = 2.46$ in ethylene/air flames (red line) and ethylene/OME_3/air flames (orange line). The difference in the infrared mass absorption coefficient between ethylene/air flames and ethylene/OME_3/air flames is shown by the black line (bottom). (For interpretation of the references to colour in this figure legend, the reader is referred to the web version of this article.)

Infrared mass absorption coefficients of carbon samples collected in the ethylene and ethylene/OME_3 with $\phi = 2.46$ are reported in the lower panel of Fig. 6 in the range 1900–900 cm^{-1}. They are mostly sensitive to the carbon skeleton and oxygen (C═O and C—O—C) functionalities, and some differences between the spectra are noticeable. These differences in the FTIR signal intensity are better shown in Fig. 6, which also illustrates the spectrum obtained as the difference between the infrared mass absorption coefficients of carbon particulate of ethylene/OME_3 flames and that of the pure ethylene flame.

The higher intensity of the 1600 cm^{-1} peak, due to the C═C stretching mode of polyaromatic systems, is clearly visible for particles collected in the flame doped with OME_3. The irregularity/dissymmetry of the aromatic moiety caused by whichever kind of ring substitution usually causes a strengthening of the 1600 cm^{-1} peak. In particular, it was found that the increase in the dipole moment associated with ring vibrations in the presence of oxygen enhances the intensity of the C═C stretching peak [57,66]. In this regard, soot sampled from the ethylene/OME_3 flame also exhibits a higher intensity of the 1720 cm^{-1} absorption peak, due to the stretching of ketonic and/or esteric C═O groups [67].

Moreover, no significant differences were found in the 1300–1000 cm^{-1} range associated with other oxygen functionalities such as ether type structures (C—O—C), as previously reported for flames doped with butanols [10] and dimethylfuran [7].

Overall, the presence of oxygen functionalities within the carbon network is in line with previous findings for other oxygenated fuels. Comparing these results with those obtained for ethanol [6], butanols [10] and furans [33], the main role of the oxygenated fuels appears to rely on the gas phase pathways: on one hand, oxygen incorporated into the fuel structure improves the decomposition/oxidation pathways, reducing the total number of precursors and hence the total number of particles produced; on the other hand, the same oxygenated group in rich conditions can lead to the formation – in small amounts – of oxy-PAHs or other large oxygen-containing molecules that can finally be included into particles. Studies are ongoing regarding the exact nature of these PAHs. The distinctive feature of OME_3 seems to be the predominance of C═O over C—O—C and OH functionalities and it is probably due to the different molecular structure of the fuel studied here with respect to other biofuels that have been investigated. The presence of C—O bonds in the fuel structure and the absence of C—C bonds probably drive the process toward the preferential formation of C═O bonds. Hence, in the case of OME_3 it seems that oxygenated functionalities are not embedded inside the aromatic network of soot particles, but are just located at the edge of the aromatic systems in the form of C═O groups. It is not possible so far to conclude which pathways lead to the presence of oxygen that is incorporated into the particles. Numerical results and the present gas-phase scheme do not include the presence and/or an active role for oxy-PAH in particle formation. Their impact on the total number of particles or even on the PSD is generally considerable less significant than other combustion and kinetic parameters. However, further studies will have to examine this topic in greater depth, also considering the significant role that the presence of oxygen can have in terms of after-treatment systems and the impact on human health [3,4].

5. Conclusions

In this study, the effects of OME_3 addition on soot particle formation in burner-stabilized premixed ethylene flames have been investigated with experiments and numerical simulations based on the CQMOM approach. 20% of the total carbon was replaced with OME_3 for four equivalence ratios – 2.01, 2.16, 2.31 and 2.46 – while the cold gas velocity was kept constant. The experiments (LII and PSD) and numerical results indicate that there is a reduction in the total number and the size

of soot particles in the OME_3-blended flame. An almost negligible effect was observed on the small condensed-phase nanostructures tracked by the LIF signal. Comparisons with experimental data for pure ethylene and blended flames indicate that the model predictivity is fair both in terms of the soot volume fraction and PSD, without any tuning for different equivalent ratios and fuel mixtures. In very rich conditions, the soot reduction due to the addition of OME_3 is underpredicted. This behavior has been hypothesized to be linked with the decomposition/oxidation of OME_3 in the early stage of combustion and subsequent formation of partially oxidized by-products and radicals. The gas-phase kinetic scheme for OME_3 taken from the literature was originally developed for different combustion conditions. To investigate the influence of the gas-phase reaction pathways on particle formation, numerical tests have been performed using, instead of OME_3, its decomposed or oxidized products to identify possible chemical pathways that lead to a reduction in the particle growth. It has been observed that a faster formation of partially oxidized products in the gas-phase kinetics may favor a further soot reduction with respect to the actual scheme; however, further research is needed to investigate the gas-phase pathways.

Finally, the effects of OME_3 addition on the chemical features of the particles, i.e. aromaticity and composition, have been analyzed in the highest equivalence ratio conditions. UV–Visible and Raman spectroscopy analysis suggest that there is a slightly lower degree of aromatization in OME_3-doped flames, probably due to the higher concentration of particles smaller than 20 nm. A higher presence of C═O functionalities was found when analyzing the FTIR spectra of the particle samples, while no significant differences were observed in C—O—C, OH, and CH functionalities. This could be attributed to the presence in the OME_3 molecule of C—O—C bonds and the total absence of C—C bonds. The presence of C═O groups associated with this fuel structure could be relevant for future studies of similar alternative fuels.

CRediT authorship contribution statement

Federica Ferraro: Conceptualization, Writing - review & editing. **Carmela Russo:** Writing - review & editing. **Robert Schmitz:** Writing - review & editing. **Christian Hasse:** Conceptualization, Funding acquisition. **Mariano Sirignano:** Conceptualization, Writing - review & editing.

Declaration of Competing Interest

The authors declare that they have no known competing financial interests or personal relationships that could have appeared to influence the work reported in this paper.

Acknowledgments

The authors gratefully acknowledge the funding by the German Federal Ministry of Education and Research (BMBF) as part of the NAMOSYN Project (project number 03SF0566R0) and, additionally, by the Clean Sky 2 Joint Undertaking under the European Union's Horizon 2020 research and innovation programme under the ESTiMatE project, grant agreement No. 821418.

References

[1] Sirignano M, Conturso M, Magno A, Di Iorio S, Mancaruso E, Maria Vaglieco B, et al. Evidence of Sub-10 nm particles emitted from a small-size diesel engine. Exp Therm Fluid Sci 2018;95:60–4. https://doi.org/10.1016/j.expthermflusci.2018.01.031.

[2] D'Anna A. Combustion-formed nanoparticles. Proc Combust Inst 2009;32:593–613. https://doi.org/10.1016/j.proci.2008.09.005.

[3] De Falco G, Colarusso C, Terlizzi M, Popolo A, Pecoraro M, Commodo M, et al. Chronic obstructive pulmonary disease-derived circulating cells release IL-18 and IL-33 under ultrafine particulate matter exposure in a caspase-1/8-independent manner. Front Immunol 2017:8. https://doi.org/10.3389/fimmu.2017.01415.

[4] Kohse-Höinghaus K, Oßwald P, Cool TA, Kasper T, Hansen N, Qi F, et al. Biofuel combustion chemistry: from ethanol to biodiesel. Angew Chemie - Int Ed 2010;49:3572–97. https://doi.org/10.1002/anie.200905335.

[5] Battin-Leclerc F, Curran H, Faravelli T, Glaude PA. Specificities related to detailed kinetic models for the combustion of oxygenated fuels components. In: Battin-Leclerc FJM, Simmie E, editors. Blurock Clean. Combust. Dev. Detail. Chem. Kinet. Model. London: Springer London; 2013. p. 93–109. https://doi.org/10.1007/978-1-4471-5307-8_4.

[6] Sirignano M, Ciajolo A, D'Anna A, Russo C. Chemical features of particles generated in an ethylene/ethanol premixed flame. Energy Fuels 2017;31:2370–7. https://doi.org/10.1021/acs.energyfuels.6b02372.

[7] Russo C, D'Anna A, Ciajolo A, Sirignano M. Analysis of the chemical features of particles generated from ethylene and ethylene/2,5 dimethyl furan flames. Combust Flame 2016;167:268–73. https://doi.org/10.1016/j.combustflame.2016.02.003.

[8] Lapuerta M, Oliva F, Agudelo JR, Boehman AL. Effect of fuel on the soot nanostructure and consequences on loading and regeneration of diesel particulate filters. Combust Flame 2012;159:844–53. https://doi.org/10.1016/j.combustflame.2011.09.003.

[9] Guan C, Cheung CS, Li X, Huang Z. Effects of oxygenated fuels on the particle-phase compounds emitted from a diesel engine. Atmos Pollut Res 2017;8:209–20. https://doi.org/10.1016/j.apr.2016.08.005.

[10] Russo C, D'Anna A, Ciajolo A, Sirignano M. The effect of butanol isomers on the formation of carbon particulate matter in fuel-rich premixed ethylene flames. Combust Flame 2019;199:122–30. https://doi.org/10.1016/j.combustflame.2018.10.025.

[11] Ess MN, Bladt H, Mühlbauer W, Seher SI, Zöllner C, Lorenz S, et al. Reactivity and structure of soot generated at varying biofuel content and engine operating parameters. Combust Flame 2016;163:157–69. https://doi.org/10.1016/j.combustflame.2015.09.016.

[12] Lapuerta M, Armas O, Rodríguez-Fernández J. Effect of biodiesel fuels on diesel engine emissions. Prog Energy Combust Sci 2008;34:198–223. https://doi.org/10.1016/j.pecs.2007.07.001.

[13] Song J, Alam M, Boehman AL, Kim U. Examination of the oxidation behavior of biodiesel soot. Combust Flame 2006;146:589–604. https://doi.org/10.1016/j.combustflame.2006.06.010.

[14] Pinzi S, Rounce P, Herreros JM, Tsolakis A, Pilar DM. The effect of biodiesel fatty acid composition on combustion and diesel engine exhaust emissions. Fuel 2013;104:170–82. https://doi.org/10.1016/j.fuel.2012.08.056.

[15] Yehliu K, Vander Wal RL, Armas O, Boehman AL. Impact of fuel formulation on the nanostructure and reactivity of diesel soot. Combust Flame 2012;159:3597–606. https://doi.org/10.1016/j.combustflame.2012.07.004.

[16] Guo Y, Ristovski Z, Graham E, Stevanovic S, Verma P, Jafari M, et al. The correlation between diesel soot chemical structure and reactivity. Carbon N Y 2020;161:736–49. https://doi.org/10.1016/j.carbon.2020.01.061.

[17] Cai L, Jacobs S, Langer R, vom Lehn F, Heufer KA, Pitsch H. Auto-ignition of oxymethylene ethers (OMEn, n = 2–4) as promising synthetic e-fuels from renewable electricity: shock tube experiments and automatic mechanism generation. Fuel 2020;264:116711. https://doi.org/10.1016/j.fuel.2019.116711.

[18] He T, Wang Z, You X, Liu H, Wang Y, Li X, et al. A chemical kinetic mechanism for the low- and intermediate-temperature combustion of Polyoxymethylene Dimethyl Ether 3 (PODE3). Fuel 2018;212:223–35. https://doi.org/10.1016/j.fuel.2017.09.080.

[19] Sanfilippo D, Patrini R, Marchionna M. Use of an oxygenated product as a substitute of gas oil in diesel engines. US 7235113 B2, 2007.

[20] Omari A, Heuser B, Pischinger S. Potential of oxymethylenether-diesel blends for ultra-low emission engines. Fuel 2017;209:232–7. https://doi.org/10.1016/j.fuel.2017.07.107.

[21] Pélerin D, Gaukel K, Härtl M, Jacob E, Wachtmeister G. Potentials to simplify the engine system using the alternative diesel fuels oxymethylene ether OME1 and OME3−6 on a heavy-duty engine. Fuel 2020;259:116231. https://doi.org/10.1016/j.fuel.2019.116231.

[22] Pellegrini L, Marchionna M, Patrini R, Florio S. Emission performance of neat and blended polyoxymethylene dimethyl ethers in an old light-duty diesel car. SAE Tech Pap 2013:2. https://doi.org/10.4271/2013-01-1035.

[23] Lumpp B, Rothe D, Pastotter C, Lämmermann R, Jacob E. Oxymethylene ethers as diesel fuel. Mtz Worldw 2011;78:34–8.

[24] Liu H, Wang Z, Wang J, He X. Improvement of emission characteristics and thermal efficiency in diesel engines by fueling gasoline/diesel/PODEn blends. Energy 2016;97:105–12. https://doi.org/10.1016/j.energy.2015.12.110.

[25] Parravicini M, Barro C, Boulouchos K. Compensation for the differences in LHV of diesel-OME blends by using injector nozzles with different number of holes: emissions and combustion. Fuel 2020;259:116166. https://doi.org/10.1016/j.fuel.2019.116166.

[26] Popp T, Lechner R, Becker M, Hebauer M, O'Connell N, Brautsch M. Potentials of OME/diesel blends for stationary power production – improving emission characteristics of a diesel CHP unit. Appl Therm Eng 2019;153:483–92. https://doi.org/10.1016/j.applthermaleng.2019.03.015.

[27] Ogawa H, Nabi N, Minami M, Miyamoto N, Kim BS. Ultra low emissions and high performance diesel combustion with a combination of high EGR, three-way catalyst, and a highly oxygenated fuel, dimethoxy methane (DMM). SAE Tech Pap 2000. https://doi.org/10.4271/2000-01-1819.

[28] Zheng Y, Tang Q, Wang T, Liao Y, Wang J. Synthesis of a green fuel additive over cation resins. Chem Eng Technol 2013;36:1951–6. https://doi.org/10.1002/ceat.201300360.

[29] Sun W, Wang G, Li S, Zhang R, Yang B, Yang J, et al. Speciation and the laminar burning velocities of poly(oxymethylene) dimethyl ether 3 (POMDME3) flames: an experimental and modeling study. Proc Combust Inst 2017;36:1269–78. https://doi.org/10.1016/j.proci.2016.05.058.
[30] Ren S, Wang Z, Li B, Liu H, Wang J. Development of a reduced polyoxymethylene dimethyl ethers (PODEn) mechanism for engine applications. Fuel 2019;238:208–24. https://doi.org/10.1016/j.fuel.2018.10.111.
[31] Tan YR, Botero ML, Sheng Y, Dreyer JAH, Xu R, Yang W, et al. Sooting characteristics of polyoxymethylene dimethyl ether blends with diesel in a diffusion flame. Fuel 2018;224:499–506. https://doi.org/10.1016/j.fuel.2018.03.051.
[32] Conturso M, Sirignano M, D'Anna A. Effect of furanic biofuels on particles formation in premixed ethylene-air flames: an experimental study. Fuel 2016;175:137–45. https://doi.org/10.1016/j.fuel.2016.02.038.
[33] Conturso M, Sirignano M, D'Anna A. Effect of 2,5-dimethylfuran doping on particle size distributions measured in premixed ethylene/air flames. Proc Combust Inst 2017;36:985–92. https://doi.org/10.1016/j.proci.2016.06.048.
[34] Salamanca M, Sirignano M, Commodo M, Minutolo P, D'Anna A. The effect of ethanol on the particle size distributions in ethylene premixed flames. Exp Therm Fluid Sci 2012;43:71–5. https://doi.org/10.1016/j.expthermflusci.2012.04.006.
[35] Salamanca M, Sirignano M, D'Anna A. Particulate formation in premixed and counter-flow diffusion ethylene/ethanol flames. Energy Fuels 2012;26:6144–52. https://doi.org/10.1021/ef301081q.
[36] Sirignano M, Salamanca M, D'Anna A. The role of dimethyl ether as substituent to ethylene on particulate formation in premixed and counter-flow diffusion flames. Fuel 2014;126:256–62. https://doi.org/10.1016/j.fuel.2014.02.039.
[37] Sirignano M, Bartos D, Conturso M, Dunn M, D'Anna A, Masri AR. Detection of nanostructures and soot in laminar premixed flames. Combust Flame 2017;176:299–308. https://doi.org/10.1016/j.combustflame.2016.10.009.
[38] D'Anna A, Sirignano M, Kent J. A model of particle nucleation in premixed ethylene flames. Combust Flame 2010;157:2106–15. https://doi.org/10.1016/j.combustflame.2010.04.019.
[39] Sirignano M, Kent J, D'Anna A. Detailed modeling of size distribution functions and hydrogen content in combustion-formed particles. Combust Flame 2010;157:1211–9. https://doi.org/10.1016/j.combustflame.2009.11.014.
[40] Salenbauch S, Sirignano M, Marchisio DL, Pollack M, Anna AD, Hasse C. Detailed particle nucleation modeling in a sooting ethylene flame using a Conditional Quadrature Method of Moments (CQMOM). Proc Combust Inst 2016;36:1–9. https://doi.org/10.1016/j.proci.2016.08.003.
[41] Salenbauch S, Sirignano M, Pollack M, D'Anna A, Hasse C. Detailed modeling of soot particle formation and comparison to optical diagnostics and size distribution measurements in premixed flames using a method of moments. Fuel 2018;222:287–93. https://doi.org/10.1016/j.fuel.2018.02.148.
[42] Yuan C, Kong B, Passalacqua A, Fox RO. An extended quadrature-based mass-velocity moment model for polydisperse bubbly flows. Can J Chem Eng 2014;92:2053–66. https://doi.org/10.1002/cjce.22006.
[43] Salenbauch S, Hasse C, Vanni M, Marchisio DL. A numerically robust method of moments with number density function reconstruction and its application to soot formation, growth and oxidation. J Aerosol Sci 2019;128:34–49. https://doi.org/10.1016/j.jaerosci.2018.11.009.
[44] Wick A, Nguyen T, Laurent F, Fox RO, Pitsch H. Modeling soot oxidation with the extended quadrature method of moments. Proc Combust Inst 2017;36:789–97. https://doi.org/10.1016/j.proci.2016.08.004.
[45] Sirignano M, D'Anna A, D'Anna A. Coagulation of combustion generated nanoparticles in low and intermediate temperature regimes: an experimental study. Proc Combust Inst 2013;34:1877–84. https://doi.org/10.1016/j.proci.2012.06.119.
[46] Zhao B, Yang Z, Johnston MV, Wang H, Anthony S, Balthasar M, et al. Measurement and numerical simulation of soot particle size distribution functions in a laminar premixed ethylene-oxygen-argon flame. Combust Flame 2003;133:173–88. https://doi.org/10.1016/S0010-2180(02)00574-6.
[47] Maricq MM. A comparison of soot size and charge distributions from ethane, ethylene, acetylene, and benzene / ethylene premixed flames 2006;144:730–43. DOI:10.1016/j.combustflame.2005.09.007.
[48] Zhao B, Yang Z, Li Z, Johnston MV, Wang H. Particle size distribution function of incipient soot in laminar premixed ethylene flames: effect of flame temperature. Proc Combust Inst 2005;30:1441–8. https://doi.org/10.1016/j.proci.2004.08.104.
[49] Thierley M, Grotheer H-H, Aigner M, Yang Z, Abid A, Zhao B, et al. On existence of nanoparticles below the sooting threshold. Proc Combust Inst 2007;31:639–47. https://doi.org/10.1016/j.proci.2006.08.035.
[50] Sgro LA, De Filippo A, Lanzuolo G, D'Alessio A. Characterization of nanoparticles of organic carbon (NOC) produced in rich premixed flames by differential mobility analysis. Proc Combust Inst 2007;31(I):631–8. https://doi.org/10.1016/j.proci.2006.08.026.
[51] Reischl GP, Mäkelä JM, Karch R, Necid J. Bipolar charging of ultrafine particles in the size range below 10 nm. J Aerosol Sci 1996;27:931–49. https://doi.org/10.1016/0021-8502(96)00026-2.
[52] Hinds WC. Properties, behavior, and measurement of airborne particles. J Aerosol Sci 1999. https://doi.org/10.1016/0021-8502(83)90049-6.
[53] Sgro LA, D'Anna A, Minutolo P. Charge distribution of incipient flame-generated particles. Aerosol Sci Technol 2010;44:651–62. https://doi.org/10.1080/02786826.2010.483701.
[54] Minutolo P, D'Anna A, D'Alessio A. On detection of nanoparticles below the sooting threshold. Combust Flame 2008;152:287–92. https://doi.org/10.1016/j.combustflame.2007.09.007.
[55] Singh J, Patterson RIA, Kraft M, Wang H. Numerical simulation and sensitivity analysis of detailed soot particle size distribution in laminar premixed ethylene flames 2006;145:117–27. DOI:10.1016/j.combustflame.2005.11.003.
[56] Sirignano M, Russo C, Ciajolo A. One-step synthesis of carbon nanoparticles and yellow to blue fluorescent nanocarbons in flame reactors. Carbon N Y 2020;156:370–7. https://doi.org/10.1016/j.carbon.2019.09.068.
[57] Russo C, Stanzione F, Tregrossi A, Ciajolo A. Infrared spectroscopy of some carbon-based materials relevant in combustion: qualitative and quantitative analysis of hydrogen. Carbon N Y 2014;74:127–38. https://doi.org/10.1016/j.carbon.2014.03.014.
[58] Sirignano M, Kent J, D'Anna A. Modeling formation and oxidation of soot in nonpremixed flames. Energy Fuels 2013;27:2303–15. https://doi.org/10.1021/ef400057r.
[59] Appel J, Bockhorn H, Wulkow M. A detailed numerical study of the evolution of soot particle size distributions in laminar premixed flames. Chemosphere 2001;42:635–45.
[60] Kruis FE, Kusters KA, Pratsinis SE, Scarlett B. A simple model for the evolution of the characteristics of aggregate particles undergoing coagulation and sintering. Aerosol Sci Technol 1993;19:514–26. https://doi.org/10.1080/02786829308959656.
[61] Sirignano M, Ciajolo A, D'Anna A, Russo C. Particle formation in premixed ethylene-benzene flames: an experimental and modeling study. Combust Flame 2019;200:23–31. https://doi.org/10.1016/j.combustflame.2018.11.006.
[62] Russo C, Apicella B, Lighty JS, Ciajolo A, Tregrossi A. Optical properties of organic carbon and soot produced in an inverse diffusion flame. Carbon N Y 2017;124:372–9. https://doi.org/10.1016/j.carbon.2017.08.073.
[63] Ferrari AC, Robertson J. Interpretation of Raman spectra of disordered and amorphous carbon. Phys Rev B 2000;61:14095–107. https://doi.org/10.1103/PhysRevB.61.14095.
[64] Russo C, Ciajolo A. Effect of the flame environment on soot nanostructure inferred by Raman spectroscopy at different excitation wavelengths. Combust Flame 2015;162:2431–41. https://doi.org/10.1016/j.combustflame.2015.02.011.
[65] Russo C, Ciajolo A, D'Anna A, Sirignano M. Modelling analysis of PAH and soot measured in a premixed toluene-doped methane flame. Fuel 2018;234:1026–32. https://doi.org/10.1016/j.fuel.2018.07.112.
[66] Fuente E, Menéndez JA, Díez MA, Suárez D, Montes-Morán MA. Infrared spectroscopy of carbon materials: a quantum chemical study of model compounds. J Phys Chem B 2003;107:6350–9. https://doi.org/10.1021/jp027482g.
[67] Akhter MS, Chughtai AR, Smith DM. The structure of hexane soot I: spectroscopic studies. Appl Spectrosc 1985;39:143–53.